BIOCHEMISTRY
including biophysical chemistry & molecular biology
Article

Biochemistry **2009,** *48,* 9503–9515 9503
DOI: 10.1021/bi900718e

Kinetic Analysis of Mad2−Cdc20 Formation: Conformational Changes in Mad2 Are Catalyzed by a C-Mad2−Ligand Complex

Latesh Lad,* Serge Lichtsteiner, James J. Hartman, Kenneth W. Wood, and Roman Sakowicz[⊥]

Cytokinetics Inc., 280 East Grand Avenue, South San Francisco, California 94080. [⊥]Current address: Gilead Sciences, 333 Lakeside Drive, Foster City, California 94404.

Received April 27, 2009; Revised Manuscript Received August 6, 2009

ABSTRACT: Structural changes in the mitotic arrest deficient protein 2 (Mad2) have been proposed to be essential for spindle checkpoint function. Current models for checkpoint activation propose that a C-Mad2−Mad1 core complex at unattached kinetochores is required for the structural activation through a process involving the interaction of two Mad2 conformers: a closed conformer bound to Mad1 or Cdc20 and an open conformer unbound to these ligands. To gain a molecular understanding of the mechanisms that accelerate the structural transition between the open and closed Mad2 conformations, we constructed a unique in vitro homogeneous Mad2 activity assay that specifically reports C-Mad2−Cdc20 formation. Using this assay we were are able to directly establish that (a) O-Mad2 transforms into a C-Mad2−Cdc20 complex >300-fold slower than unliganded C-Mad2, (b) a stable C-Mad2−Mad1 core complex catalyzes the transformation of O-Mad2 into a Cdc20-bound C-Mad2 complex, (c) a C-Mad2−Cdc20 complex can promote its own transformation of O-Mad2 into a Cdc20-bound C-Mad2 complex, and (d) the binding interaction between unliganded C-Mad2 and Cdc20 cannot be catalyzed by a C-Mad2−Mad1 core complex. Our data are consistent with the "Mad2 template" catalytic model in which a C-Mad2 template facilitates the binding of O-Mad2 to Cdc20 and supports a mechanism of C-Mad2−Cdc20 formation away from Mad1 containing kinetochores. Furthermore, our unique homogeneous Mad2 assay could be translated into a screening platform to identify small molecule drug-like compounds that directly modulate C-Mad2−Cdc20 formation.

Cells maintain fidelity of chromosome segregation and inheritance by employing a surveillance mechanism called the spindle assembly checkpoint (SAC) to sense improper attachment of sister chromatids to the mitotic spindle before their separation during mitosis (*1*−*3*). The ubiquitin ligase activity of the anaphase promoting complex, or cyclosome (APC/C), is required to trigger anaphase and mitotic exit. SAC targets Cdc20, an activator of the APC/C, in order to prevent premature activation of the APC/C until all sister chromatid pairs are properly aligned at the metaphase plate (*4*). Upon biorientation of all sister chromatid pairs, the SAC is satisfied and switches off, leading to APC/C activation and initiation of sister chromatid separation in anaphase (*4*). Critical to the SAC is the interaction of Mad2[1] with Cdc20 (*5*, *6*). During mitosis Mad2 is continuously recruited to kinetochores and then released in a form that directly binds Cdc20 and reduces APC/C ubiquitination activity until the SAC is satisfied (*4*, *7*−*10*). However, mutations in the Mad2-binding site of Cdc20 have been shown to abrogate the SAC (*5*, *6*, *10*−*12*). Binding of Mad2 to Cdc20 requires the coiled−coil protein Mad1, an upstream regulator of Mad2 that binds to Mad2 throughout the cell cycle (*13*−*15*). Although the sequences of Cdc20 and Mad1 are otherwise different, they share a conformationally extended segment which fits into the ligand-binding domain of Mad2 (*15*). A series of biochemical and structural studies have explored the mechanism of Mad2 binding to either Cdc20 or Mad1 and revealed that Mad2 adopts two conformations (*15*−*19*). This conformational switch that occurs within Mad2 is believed to be central to its regulation of the SAC (*20*−*26*).

The two distinct conformations of Mad2, named open Mad2 (O-Mad2) and closed Mad2 (C-Mad2), differ from one another in the position of the C-terminal tail which is composed of two β-strands and is commonly referred to as the "safety belt". When bound to Mad1 or Cdc20 the safety belt is found in its closed conformation, in which the two β-strands of Mad2 trap Mad1 or Cdc20 in the binding pocket (*15*, *19*). However, for O-Mad2 the safety belt occupies a resting position at the opposite end of an exposed β-sheet (*15*−*17*). Another important difference between the two Mad2 conformers is their oligomeric state. Early studies have shown that bacterially expressed Mad2 protein existed in both monomeric and dimeric forms in the absence of any ligand or modifications (*10*). Interestingly, the Mad2 dimer, but not the monomer, was shown to be active in APC/C inhibition in *Xenopus* egg extracts (*10*). Structural studies combined with site-directed mutagenesis revealed that the monomeric form of Mad2 was O-Mad2 (*16*−*18*), whereas the dimeric form predominantly contained one C-Mad2 molecule and one O-Mad2 molecule which resulted in an asymmetric O−C Mad2 dimer (*18*, *27*). Before SAC activation, most Mad2 is found in the monomeric open form and is not bound to Cdc20, but upon SAC activation O-Mad2 binds to Cdc20 and switches to the closed

*To whom correspondence should be addressed. E-mail: llad@cytokinetics.com. Phone: (650) 624-3000. Fax: (650) 624-3010.

[1]Abbreviations: Mad2, mitotic arrest deficient protein 2; O-Mad2, open conformation of Mad2; C-Mad2, closed conformation of Mad2; C*-Mad2, unliganded C-Mad2; $Mad2^{RQ}$, R133E:Q134A double mutant of Mad2; O−C Mad2, asymmetric O-Mad2:C-Mad2 dimer; C−C Mad2, symmetric C-Mad2:C-Mad2 dimer; FP, fluorescence polarization; dFP, delta fluorescence polarization; TRCdc20, synthetic $Cdc20^{111-138}$ peptide coupled to Texas Red; SEC, size-exclusion chromatography; ITC, isothermal titration calorimetry; CENP-E, centromere-associated protein E; FRAP, fluorescence recovery after photobleaching; mp, millipolar.

© 2009 American Chemical Society
Published on Web 08/31/2009

form (*15*, *17*). FRAP studies demonstrated that two distinct pools of Mad2 associate with kinetochores (*7*, *9*). Mad1 at kinetochores was found to be nonexchangeable whereas the two pools of kinetochore-associated Mad2 either cycle on and off or are stably bound at the kinetochores (*7*, *9*). More recently, elegant in vitro FRAP studies were able to directly demonstrate that O-Mad2 is recruited by a second stably associated Mad2 bound in the closed conformation to Mad1 and predicted that conformational dimerization of Mad2 was essential for its activation at the SAC (*28*).

At present two related but distinct models for how Mad2 is activated at the SAC, "Mad2 template" and "two-state" models, have been proposed. Both models are based upon the following three observations. First, Mad2 is able to adopt at least two distinct conformations (O-Mad2 and C-Mad2). Second, C-Mad2 forms structurally equivalent complexes with its kinetochore receptor Mad1 and its spindle checkpoint target Cdc20. Lastly, O-Mad2 and C-Mad2 conformers engage to form an asymmetric O−C Mad2 complex. Both the "template" and "two-state" models propose that a stable C-Mad2−Mad1 core complex at unattached kinetochores recruits O-Mad2 from the cytosol to the kinetochore. O-Mad2 and C-Mad2 bound to Mad1 engage in the form of an asymmetric dimer. Since an "always open" Mad2 does not bind Cdc20, however, partnering of O-Mad2 with C-Mad2 is proposed to act as a platform for Mad2 conversion required to bind Cdc20 and subsequent formation of a C-Mad2−Cdc20 complex. This aspect of both models has been tested and shown that a C-Mad2−Mad1 complex can convert O-Mad2 into a C-Mad2−Cdc20 complex (*27*, *29*, *30*). The template model also proposes that a C-Mad2−Cdc20 complex may then propagate the mechanism of O-Mad2 conversion away from the C-Mad2−Mad1 containing kinetochores through an autocatalytic loop; that is, the C-Mad2−Cdc20 complex represents a structural copy of the C-Mad2−Mad1 core complex and therefore might be endowed with similar catalytic properties (*20*). The "two-state" model assumes that conformational catalysis only occurs at the kinetochores and therefore identifies an unliganded C-Mad2 (C*-Mad2) as the active Mad2 species generated from conformational dimerization which then binds Cdc20 (*26*, *27*). Mathematical modeling and stimulations have also come to conflicting conclusions about the two models for Mad2 activation. Some theoretical studies do not favor O-Mad2 conversion away from kinetochores as proposed by the "template" model since it would force the cell to be permanently arrested with most of the Cdc20 sequestered by Mad2 (*31*, *32*). However, other studies argue that the contribution of the autocatalytic loop to the SAC is either negligible (*33*) or significant (*30*).

To gain a precise molecular understanding of the mechanisms that accelerate the structural transition between O-Mad2 and C-Mad2 conformations at the SAC, we developed a unique fluorescence polarization (FP) assay that specifically reports C-Mad2−Cdc20 formation. FP is a quantitative, solution-based, homogeneous assay format which measures the rate of molecular rotation of a fluorescently labeled ligand. FP is related to the molecular sizes and thus the differing rotational properties of small versus large molecules; the smaller the size and the faster the rotation, the lower the FP value (*34*). In our FP assay we used a small fluorescently labeled synthetic peptide encompassing residues 111−138 of human Cdc20 ($Cdc20^{111-138}$) that has been reported to be a stronger Mad2 ligand than full-length Cdc20 (*35*, *36*) and monitored the binding of this peptide to the larger protein, Mad2. Full-length Mad2 has a large molecular mass (~25 kDa) compared to $Cdc20^{111-138}$ (~3 kDa), and therefore binding of Mad2 to the fluorescently labeled synthetic $Cdc20^{111-138}$ peptide will result in a significant change in FP values. This phenomenon provides a large signal window and high sensitivity for studying the C-Mad2−Cdc20 interaction. In this work we are able to show that our novel FP assay serves as a real time sensor of Mad2 conformation. Using this assay we are also able to provide a detailed kinetic and mechanistic description for C-Mad2−Cdc20 formation and demonstrate that both a C-Mad2−Mad1 and C-Mad2−Cdc20 complexes selectively catalyzed the binding of O-Mad2 to Cdc20 and not unliganded C-Mad2 to Cdc20.

EXPERIMENTAL PROCEDURES

Materials. Peptides corresponding to residues 111−138 of human Cdc20 (EHQKAWALNLNGFDVEEAKILRLSGKPQ), which represent the Mad2 binding domain, were custom synthesized (Sigma Genosys) with or without an N-terminal fluorescent label (Texas Red).

Expression and Purification. Full-length human Mad2 proteins (residues 1−205) were expressed in *Escherichia coli* BL21(DE3) as N-terminal 6-His fusion proteins at 16 °C for 12 h after induction with 0.1 mM IPTG. Bacterial cells were lysed with a microfluidizer (Microfluidics Corp.) in lysis buffer [50 mM sodium phosphate (pH 7.8), 300 mM NaCl, 5 mM imidazole, 8 mM β-mercaptoethanol, and EDTA-free protease inhibitor cocktail (Roche Diagnostics)], and the resulting proteins were purified using Ni-NTA agarose affinity chromatography with an elution buffer consisting of 50 mM sodium phosphate (pH 6.0), 300 mM NaCl, 10% glycerol, and 150 mM imidazole. Mad2 conformers were isolated by ion-exchange chromatography (Source 15Q resin; GE Healthcare) using a NaCl gradient (0−500 mM) in Q-buffer containing 20 mM Tris-HCl (pH 8), 50 mM NaCl, 0.25 mM EDTA, and 1 mM DTT. O-Mad2 eluted at a lower salt concentration (~150 mM NaCl), whereas unliganded C-Mad2 eluted at a higher salt concentration (~260 mM NaCl). The two Mad2 conformations of Mad2 were pooled separately and further purified by a Superdex-75 column (Amersham) equilibrated with 20 mM Tris-HCl (pH 8), 100 mM NaCl, 0.25 mM EDTA, and 1 mM DTT.

We generated a construct to coexpress the Mad2 binding domain of human Mad1 (residues 485−718) with full-length human Mad2 containing an N-terminal 6-His (C-Mad2−$Mad1^{485-718}$) as previously described (*37*). The C-Mad2−$Mad1^{485-718}$ core complex was expressed in *E. coli* BL21(DE3) at 30 °C for 12 h after induction with 0.1 mM IPTG. Bacterial cells were lysed with a microfluidizer (Microfluidics Corp.) in lysis buffer [50 mM Tris-HCl (pH 8.0), 150 mM NaCl, 5% glycerol, 5 mM imidazole, 8 mM β-mercaptoethanol, and EDTA-free protease inhibitor cocktail (Roche Diagnostics)], and the resulting complex was further purified using Ni-NTA agarose affinity chromatography with an elution buffer consisting of 50 mM Tris-HCl (pH 8.0), 150 mM NaCl, 5% glycerol, and 150 mM imidazole. Low molecular weight oligomers of Mad2 were removed by gel filtration [Superdex-200 (Amersham) equilibrated with 20 mM Tris-HCl (pH 8), 200 mM NaCl, 0.25 mM EDTA, and 1 mM DTT] whereas high molecular weight oligomers were removed by ion-exchange chromatography (Source 15Q resin; GE Healthcare) using a NaCl gradient (0−500 mM) in Q-buffer containing 20 mM Tris-HCl (pH 8.0), 50 mM NaCl, and 1 mM DTT. Fractions containing the

C-Mad2−Mad1$^{485-718}$ core complex were pooled and then incubated with an excess of unlabeled Cdc20$^{111-138}$ synthetic peptide (5:1 ratio of Cdc20/C-Mad2−Mad1$^{485-718}$) for 1 h at room temperature followed by an overnight incubation at 4 °C in order to remove any associated Mad2 molecules from the C-Mad2−Mad1$^{485-718}$ core complex. The C-Mad2−Mad1$^{485-718}$ core complex was separated from C-Mad2−Cdc20$^{111-138}$ by a second Superdex-200 column (Amersham) equilibrated with 20 mM Tris-HCl (pH 8), 200 mM NaCl, 0.25 mM EDTA, and 1 mM DTT. The motor domain of CENP-E (amino acids 2−340) was expressed in *E. coli* BL21(DE3) as a C-terminal 6-His fusion protein. Bacterial cells were lysed with a microfluidizer (Microfluidics Corp.) in lysis buffer [50 mM Tris-HCl, 50 mM KCl, 10 mM imidazole, 2 mM $MgCl_2$, 8 mM β-mercaptoethanol, and 0.1 mM ATP (pH 7.4)], and the resulting protein was further purified using Ni-NTA agarose affinity chromatography with an elution buffer consisting of 50 mM PIPES, 300 mM imidazole, 50 mM KCl, 2 mM $MgCl_2$, 8 mM β-mercaptoethanol, and 0.1 mM ATP (pH 6.8).

Isothermal Titration Calorimetry (*ITC*). ITC was performed with a VP-ITC titration calorimeter (MicroCal Inc.) at 20 °C. Calorimetric measurements were carried out with unliganded C-Mad2 and the synthetic peptide corresponding to residues 111−138 of human Cdc20 (Cdc20$^{111-138}$). For each titration experiment, 3 mL of 20 μM protein solution in a buffer containing 20 mM Tris-HCl (pH 8), 100 mM NaCl, 0.25 mM EDTA, and 0.5 mM TCEP was added to the calorimeter cell. Cdc20$^{111-138}$ (1 mM) in the exact same buffer was injected with 30 portions of 10 μL with an injection syringe. Binding parameters were evaluated using a single site binding model (Origin).

Analytical Size-Exclusion Chromatography (*SEC*). Analytical SEC was carried out on a SMART system (Amersham Pharmacia Biotech) with a Superdex-200 PC 3.2/30 column in a buffer containing 20 mM Tris-HCl (pH 8), 100 mM NaCl, 0.25 mM EDTA, and 1 mM DTT. Twenty microliter protein samples were separated by SEC at flow rate of 40 μL/min.

Fluorescent Polarization Measurements. FP measurements were performed in either a M5 SpectraMax plate reader (Molecular Devices) or a stopped-flow instrument (SF-61 DX2; Hi-Tech Scientific) set up in a T format. All kinetic experiments measuring binding between unliganded C-Mad2 and TRCdc20$^{111-138}$ were conducted in the stopped-flow instrument. The excitation wavelength was 584 nm, and the emission filter cutoff was 590 nm. For each data point, stopped-flow traces were collected in triplicate and averaged before fitting. All other kinetic and binding experiments were performed in the plate reader using a 96-well plate [Corning (3694) black plate]. FP values (mp) on the plate reader were determined using a λ_{ex} = 584 nm, a λ_{em} = 614 nm, and a cutoff filter wavelength set at 610 nm. For equilibrium binding, TRCdc20$^{111-138}$ (75 nM) was mixed with different concentrations of unliganded C-Mad2 (0.05−20 μM) in a 96-well plate and incubated at room temperature for 20 min before reading. All kinetic and equilibrium binding experiments were performed at room temperature in 20 mM Tris-HCl (pH 8), 100 mM NaCl, 0.25 mM EDTA, 50 μg/mL bovine γ-globulin, 50 ppm antifoam, and 1 mM DTT. Data for equilibrium binding using TRCdc20$^{111-138}$ as the ligand were fitted to the quadratic equation:

$$[RL] = \frac{(K_d + [L] + [R]) - \sqrt{(K_d + [L] + [R])^2 - 4[L][R]}}{2} \quad (1)$$

where K_d is the equilibrium dissociation constant, [R] is Mad2 concentration, [L] is the ligand concentration (TRCdc20$^{111-138}$), and [RL] is the concentration of the C-Mad2−TRCdc20$^{111-138}$ complex (*38*). All data analysis and fitting were done using equations in GraFit (version 5.0.11; Erithacus Software Ltd.).

Non-FP C-Mad2−Cdc20 Assay. C-Mad2−TRCdc20$^{111-138}$ formation was determined by measuring the endogenous fluorescence (fluorescence intensity) of TRCdc20$^{111-138}$ bound to Mad2 at various time intervals after spin column gel filtration. Mad2 (1 μM) was incubated with TRCdc20$^{111-138}$ (1 μM) in the presence or absence of the C-Mad2−Mad1$^{485-718}$ core complex (100 nM) at various time intervals in 20 mM Tris-HCl (pH 8), 100 mM NaCl, 0.25 mM EDTA, 50 μg/mL bovine γ-globulin, 50 ppm antifoam, and 1 mM DTT. Reactions were gel filtered by centrifugation (1500*g* for 2 min) using zebra desalt spin columns (Pierce) to remove unbound TRCdc20$^{111-138}$. The resulting C-Mad2−TRCdc20$^{111-138}$ supernatant was transferred to a 96-well plate to measure the fluorescence intensity of TRCdc20$^{111-138}$ bound to Mad2. End point fluorescence intensity TRCdc20$^{111-138}$ measurements were determined at room temperature and performed in a Gemini XS plate reader (Molecular Devices). TRCdc20$^{111-138}$ fluorescence was monitored at λ_{ex} = 584 nm with a cutoff filter wavelength set at 610 nm.

RESULTS

Mad2, C-Mad2−Mad1$^{485-718}$, and Cdc20$^{111-138}$ Functional Characterization. For our studies we expressed full-length human Mad2, whereas for the C-Mad2−Mad1 core complex we coexpressed the C-terminal region of human Mad1 [residues 485−718 (Mad1$^{485-718}$)] and full-length human Mad2. Our Cdc20 ligand was a synthetic peptide encompassing residues 111−138 of human Cdc20, a stronger Mad2 ligand than full-length Cdc20 (*35*, *36*). We used size-exclusion chromatography (SEC) and isothermal titration calorimetry (ITC) to assess protein purity, activity, and functionality. Mad2 forms oligomers due to the interaction of its two conformers, O-Mad2 and C-Mad2 (*18*, *27*). For simplicity, in the absence of ligands, the "empty" form of C-Mad2 will be referred to as unliganded C-Mad2 and be represented as C*-Mad2 in the figures presented in this paper. During protein purification we used anion-exchange chromatography to separate and isolate O-Mad2 and unliganded C-Mad2. Based on previous reports, O-Mad2 exists as a monomer whereas unliganded C-Mad2 exists as a dimer in the absence of its ligands, Cdc20 or Mad1. The C-Mad2−Mad1$^{485-718}$ core complex exists as a stable asymmetric tetramer (two copies of Mad2 interact with two copies of Mad1) (*19*, *20*). When we compared the elution profiles of our purified O-Mad2, unliganded C-Mad2, and C-Mad2−Mad1$^{485-718}$ core complex from a Superdex-200 size-exclusion chromatography column (Figure 1A), we found that the elution profiles of our proteins agree with previous reports (*20*). O-Mad2 eluted from the gel filtration column with an apparent molecular mass of ~25 kDa consistent with it being a monomer, whereas unliganded C-Mad2 eluted with an apparent molecular mass of ~50 kDa consistent with it being a dimer. On the basis of the results from a recent structural study, which revealed that unliganded C-Mad2 predominantly exists as an asymmetric Mad2 dimer (O−C Mad2) (*27*), we assumed that the unliganded C-Mad2 used in this study also predominately exists as O−C Mad2. The C-Mad2−Mad1$^{485-718}$ core complex eluted from the gel filtration

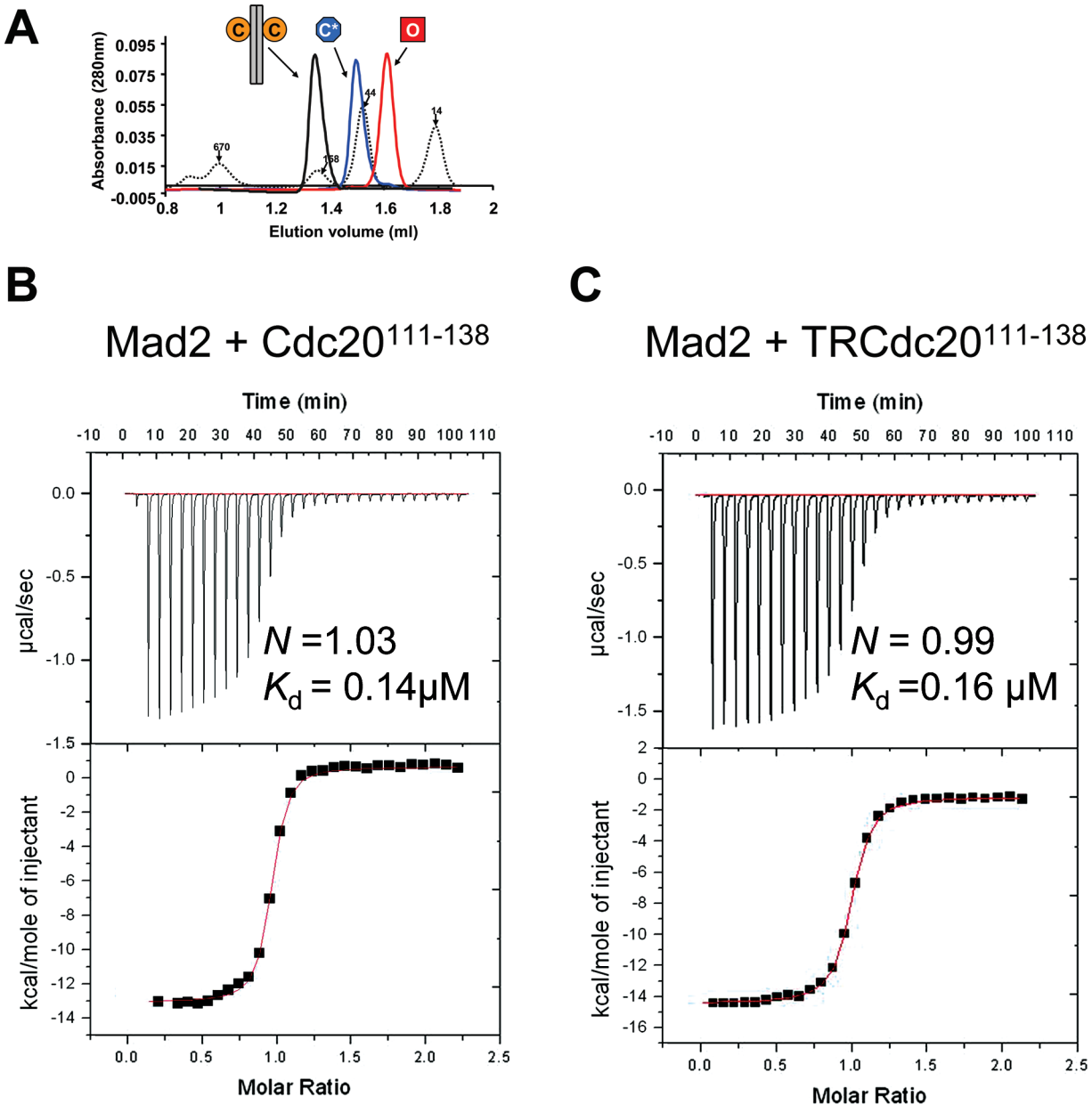

FIGURE 1: Characterization of the components of the Mad2 FP assay. (A) SEC elution profiles from a Superdex-200 PC 3.2/30 column monitored at A_{280nm} for O-Mad2 (red line), unliganded C-Mad2, represented as C*-Mad2 in the figure (blue line), and C-Mad2−Mad1$^{485-718}$ (black line). Molecular weight markers are represented as a black dotted line. Final protein concentrations for Mad2 and C-Mad2−Mad1$^{485-718}$ were 4 μM. (B) ITC analysis of the binding between unliganded C-Mad2 and unlabeled Cdc20$^{111-138}$ peptide. The dissociation constant (K_d) and the stoichiometry (N) of binding are indicated. (C) ITC analysis of the binding between unliganded C-Mad2 and TRCdc20$^{111-138}$ peptide. The dissociation constant (K_d) and the stoichiometry (N) of binding are indicated. All experiments were conducted at room temperature in 20 mM Tris-HCl (pH 8), 100 mM NaCl, 0.25 mM EDTA, and 1 mM DTT or 0.5 mM TCEP.

column as a single peak with an apparent MW of ~160 kDa, which was higher than the expected MW (~110 kDa) (Figure 1A). This deviation has been previously reported and attributed to the elongated shape of the C-Mad2−Mad1 core complex (*20*).

We used ITC to measure binding between unliganded C-Mad2 and our synthetic Cdc20$^{111-138}$ peptide, establishing that our purified Mad2 protein was functional and therefore able to bind its substrate and that coupling of a fluorescent probe (Texas Red) on the N-terminus of our Cdc20 peptide did not perturb its binding affinity with Mad2. It had been previously shown that the interaction of Mad2 with Cdc20 peptides gave rise to a simple 1:1 complex with an apparent K_d ranging from 0.1 to 0.6 μM (*19*, *39*). Our ITC experiments revealed that Cdc20$^{111-138}$ peptide bound unliganded C-Mad2 with a dissociation constant (K_d) of 0.14 ± 0.003 μM and a binding stoichiometry (N) of 1.03 ± 0.04 (Figure 1B), which are comparable with previously reported values using a similar length peptide (*19*). Furthermore, the coupling of the Texas Red fluorescent dye on the N-terminus of Cdc20$^{111-138}$ (TRCdc20$^{111-138}$) did not perturb the binding affinity or alter the binding stoichiometry between Cdc20$^{111-138}$ and unliganded C-Mad2 (K_d = 0.16 ± 0.001 μM, N = 0.99 ± 0.07, Figure 1C).

A New Assay To Specifically Measure C-Mad2−Cdc20 Formation. In the absence of ligand (Cdc20 or Mad1) Mad2 exists in two forms. It is believed that unliganded C-Mad2 readily binds to its Mad2 ligands to form a C-Mad2−ligand complex whereas O-Mad2 binds Cdc20 significantly more slowly (*17*, *29*, *30*).

For this reason, initial studies monitoring the formation of a C-Mad2−TRCdc20$^{111-138}$ complex by equilibrium binding were performed using unliganded C-Mad2. The time course for reaching equilibrium was investigated by monitoring the binding of unliganded C-Mad2 (10 μM) to TRCdc20$^{111-138}$ (75 nM) over 1 h. The binding reached equilibrium in less than 20 min (data not shown). During the time course, the total fluorescence intensity levels remained similar, indicating a lack of significant quenching upon formation of the C-Mad2−TRCdc20$^{111-138}$ complex. Measurement of the equilibrium dissociation constant was then performed by titrating either unliganded C-Mad2 or the motor domain of the centromere-associated protein E (CENP-E). CENP-E is a plus end directed microtubule mitotic kinesin motor protein known to be an essential kinetochore component that directly contributes to the capture and stabilization of spindle microtubules during mitosis (*40*). CENP-E should not bind Cdc20 and therefore was used as an internal control during the equilibrium binding experiment. Our ITC experiments revealed that the binding affinity of TRCdc20$^{111-138}$ for unliganded C-Mad2 was in the nanomolar range (K_d = 0.16 μM or 160 nM, Table 2); thus, formation of the C-Mad2−TRCdc20$^{111-138}$ complex may lead to free ligand depletion. To account for this possible binding behavior, the binding data (mp) were transformed and fit to a quadratic equation (eq 1) that considers ligand depletion. A binding isotherm obtained at 75 nM TRCdc20$^{111-138}$ concentration is shown in Figure 2A and has a calculated K_d = 0.17 ± 0.01 μM, which is comparable to our ITC data. We repeated the experiment using several other TRCdc20$^{111-138}$ concentrations (50, 150, and 250 nM) and found that the K_d values did not change as a function of the ligand (TRCdc20$^{111-138}$) concentration when fitted to the quadratic equation. We also observed no binding of TRCdc20$^{111-138}$ to CENP-E, indicating that our labeled Cdc20 peptide specifically binds to Mad2, and the resulting FP signal accurately reports the formation of a C-Mad2−TRCdc20$^{111-138}$ complex (Figure 2A).

Kinetics of C-Mad2−Cdc20 Formation: O-Mad2 Binds Cdc20 300-Fold More Slowly Than Unliganded C-Mad2. Having established that fluorescence polarization of TRCdc20$^{111-138}$ specifically reports C-Mad2−TRCdc20$^{111-138}$ formation, we then kinetically measured the binding between Mad2 and TRCdc20$^{111-138}$. It has been shown that the oligomeric state of C-Mad2 bound to Cdc20 is dependent upon Cdc20 concentration (*41*). We wanted to establish a simplified kinetic platform to characterize the binding between Mad2 and Cdc20$^{111-138}$ and therefore used a 1:1 Mad2/Cdc20$^{111-138}$ ratio. Based on previous reports a 1:1 Mad2/Cdc20$^{111-138}$ ratio should result in an O−C Mad2−Cdc20$^{111-138}$ complex (Mad2 dimer bound to Cdc20$^{111-138}$) (*18*, *41*). We confirmed the formation of an O−C Mad2−Cdc20$^{111-138}$ complex by incubating a 1:1 ratio of Mad2/TRCdc20$^{111-138}$ for ~3 h at 37 °C and then evaluating the elution profile from a Superdex-200 size-exclusion chromatography column (Figure 2B). As shown previously in Figure 1A, O-Mad2 alone exists as a monomer; however, after incubation with an equimolar amount of TRCdc20$^{111-138}$ Mad2 eluted with a Stokes radius larger than O-Mad2 or unliganded C-Mad2 alone, but compatible with the molecular mass (~50 kDa) of a Mad2 dimer (Figure 2B).

We used our FP assay to monitor the binding of TRCdc20$^{111-138}$ (1 μM) to an equimolar amount of Mad2 [either unliganded C-Mad2 (1 μM) or O-Mad2 (1 μM)], in real time, as an increase in FP signal. The time-dependent increase in FP corresponds to the formation of C-Mad2−TRCdc20$^{111-138}$. The kinetics of C-Mad2−TRCdc20$^{111-138}$ formation revealed

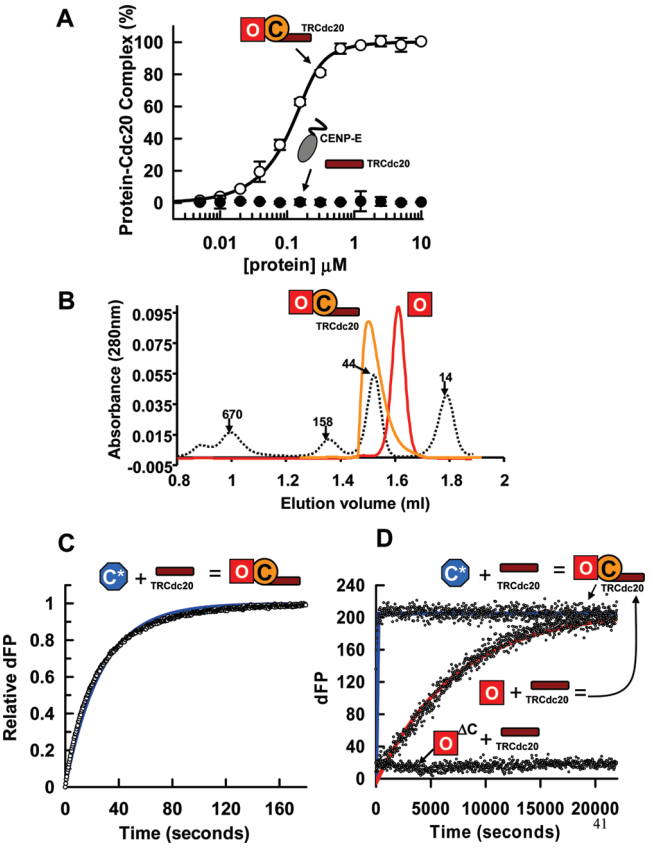

FIGURE 2: Equilibrium and kinetic binding of Mad2 and TRCdc20$^{111-138}$. (A) Equilibrium binding of TRCdc20$^{111-138}$ to either unliganded C-Mad2 or the motor domain of CENP-E in an FP assay. The equilibrium dissociation constant was measured by titrating either unliganded C-Mad2 or CENP-E at a fixed concentration of TRCdc20$^{111-138}$ (75 nM). The binding data (mP) were transformed and fit to a quadratic equation. (B) Elution profiles of O-Mad2 incubated in the presence or absence of Cdc20$^{111-138}$ from a Superdex-200 PC 3.2/30 column monitored at A_{280nm}. O-Mad2 alone elutes as a monomer (red line) whereas O-Mad2 incubated in presence of an equimolar amount of Cdc20$^{111-138}$ elutes as a dimer (yellow line). Molecular weight markers are represented as a black dotted line. Final protein concentrations for Mad2 and Cdc20$^{111-138}$ were 4 μM. (C) Representative stopped-flow kinetic trace monitoring the binding between C*-Mad2 (1 μM) and TRCdc20$^{111-138}$ (1 μM). Data were fitted to a single exponential equation (blue line) in order to obtain a first-order rate constant (k_{obs} (s^{-1})). (D) Kinetic traces recorded on a plate reader showing that O-Mad2 binds TRCdc20$^{111-138}$ more slowly than C*-Mad2, and Mad2$^{\Delta C}$ cannot bind TRCdc20$^{111-138}$. Protein concentrations for the reactions were 1 μM O-Mad2, 1 μM C*-Mad2, and 1 μM TRCdc20$^{111-138}$. Kinetic traces were fit to a single exponential equation (red line for O-Mad2 and blue line for C*-Mad2) in order to obtain a first-order rate constant (k_{obs} (s^{-1})).

that unliganded C-Mad2 rapidly binds TRCdc20$^{111-138}$ with an observed rate (k_{obs}) of 0.037 s^{-1} (Figure 2C) whereas O-Mad2 binds TRCdc20$^{111-138}$ ~300-fold more slowly (k_{obs} = 0.00012 s^{-1}) (Figure 2D). Interestingly, the O-Mad2 kinetic trace deviated from a typical monophasic process and appeared somewhat sigmoidal with an initial lag of ~250 s. Moreover, when we increased the concentration of O-Mad2, the kinetic traces became less sigmoidal and more monophasic, which coincided with the absence of the lag phase initially observed at an equimolar Mad2/TRCdc20$^{111-138}$ concentration (Supporting Information Figure S1). The observed rates for the formation of C-Mad2−TRCdc20$^{111-138}$ showed a linear dependence on O-Mad2 concentration between 1 and 8 μM (Supporting

Table 1: Properties of Mad2 and Mad2 Mutants

Mad2 name	mutation(s)	allowed conformation	Mad1 or Cdc20 binding	Mad2 dimerization	relevant ref for mutant
wild type	none	O-Mad2, C-Mad2	yes	yes	
$Mad2^{\Delta C}$	10-residue C-terminal deletion	O-Mad2	no	yes	*10*, *16*, *17*, *28*, *37*
$Mad2^{RQ}$	Arg133 to Glu, Gln134 to Ala	O-Mad2, C-Mad2	yes	no	*18*, *20*, *27*, *29*
$Mad2^{RQ\text{-}\Delta C}$	Arg133 to Glu, Gln134 to Ala, 10-residue C-terminal deletion	O-Mad2	no	no	*18*, *20*, *29*

Information Figure S1, inset) and had a calculated second-order rate constant of 5.3×10^{-5} μM s^{-1} compared to 3.7×10^{-2} μM s^{-1} for unliganded C-Mad2 (Supporting Information Figure S1, inset). To corroborate the Mad2 time-dependent FP signal observed during the binding between $TRCdc20^{111-138}$ and O-Mad2 or C*-Mad2, we used a Mad2 mutant with selectively altered functions (Table 1). $Mad2^{\Delta C}$ is unable to bind Mad1 or Cdc20 because a 10-residue C-terminal deletion locks the safety belt in the O-Mad2 conformation. Incubation of $Mad2^{\Delta C}$ with $TRCdc20^{111-138}$ did not produce a time-dependent FP signal change (Figure 2D), confirming that $Mad2^{\Delta C}$ cannot bind Cdc20 and, also, that a time-dependent increase in FP signal represents C-Mad2−$TRCdc20^{111-138}$ complex formation.

C-Mad2−Mad1 Core Complex Catalyzes O-Mad2 Binding to Cdc20. At present there are two related but distinct models that describe Mad2 activation in the SAC (*20*, *26*). Both models, the "Mad2 template" and the "two-state" model, propose that a stable C-Mad2−Mad1 receptor recruits O-Mad2 to the kinetochore and acts as a platform for the Mad2 conversion required to bind Cdc20. Recent studies using either image-based binding assays to report Mad2−Cdc20 formation (*30*) or isolated chromosomes and a large array of purified mitotic checkpoint components to generate an APC/C inhibitor (*29*) have demonstrated that the conversion of O-Mad2 to C-Mad2−Cdc20 is catalyzed by a C-Mad2−Mad1 complex. To confirm these results using our FP assay and our purified proteins, we kinetically monitored the binding between O-Mad2 (1 μM) and $TRCdc20^{111-138}$ (1 μM) in the presence of substoichiometric concentrations of C-Mad2−$Mad1^{485-718}$ (0−200 nM). Figure 3A shows representative traces for O-Mad2 binding to $TRCdc20^{111-138}$ in the presence of C-Mad2−$Mad1^{485-718}$. Under these experimental conditions we are able to confirm that a C-Mad2−Mad1 core complex (C-Mad2−$Mad1^{485-718}$) was able to catalyze the transformation of O-Mad2 into a C-Mad2−$TRCdc20^{111-138}$ complex. The kinetic traces generated in the presence of C-Mad2−$Mad1^{485-718}$ were monophasic and fitted to a single exponential function. The observed rates for the formation of a C-Mad2−$TRCdc20^{111-138}$ complex (k_{obs}) were linearly dependent on C-Mad2−$Mad1^{485-718}$ concentration between 0 and 200 nM (Figure 3A, inset) and yielded a second-order rate constant of 3.3×10^{-3} μM s^{-1}. Interestingly, when we repeated the experiment using unliganded C-Mad2 instead of O-Mad2, we did not observe a catalytic increase in the rate of C-Mad2−$TRCdc20^{111-138}$ formation in the presence of C-Mad2−$Mad1^{485-718}$ (Supporting Information Figure S2). As a control, we also measured binding between $Mad2^{\Delta C}$ (1 μM) and $TRCdc20^{111-138}$ (1 μM) in the presence of substoichiometric concentrations of C-Mad2−$Mad1^{485-718}$ (0−200 nM). Although $Mad2^{\Delta C}$ is unable to bind Mad1 or Cdc20, it retains the ability to bind C-Mad2 and therefore can be recruited by a C-Mad2−Mad1 complex (Table 1). In Figure 3A, inset, we show that increasing concentrations of C-Mad2−$Mad1^{485-715}$ are unable to stimulate the binding between $Mad2^{\Delta C}$ and $TRCdc20^{111-138}$, indicating that the catalytic effect observed on O-Mad2 is not an assay artifact.

The binding affinity between Mad2 and Mad1 in the C-Mad2−$Mad1^{485-718}$ complex is extremely high and very stable based on studies conducted with high salt (up to 2 M NaCl) and chaotropic agents (up to 4 M urea) (*37*). Thus, as control, when we kinetically monitored the binding between C-Mad2−$Mad1^{485-718}$ (0−200 nM) and $TRCdc20^{111-138}$ (1 μM) in the absence of O-Mad2, it was not surprising that we observed almost no increase in FP signal compared to the catalyzed reaction (Figure 3B). This indicates that our C-Mad2−$Mad1^{485-718}$ core complex does not contain loosely associated Mad2 oligomers and our synthetic $Cdc20^{111-138}$ peptide does not cause release of Mad2 from Mad1 in order to form a C-Mad2−$TRCdc20^{111-138}$ complex. This is consistent with our C-Mad2−$Mad1^{485-718}$ purification protocol. To ensure we purified a C-Mad2−$Mad1^{485-718}$ complex devoid of any Mad2 oligomers, we incubated the core complex with excess $Cdc20^{111-138}$. The C-Mad2−$Mad1^{485-718}$ complex was separated from excess $Cdc20^{111-138}$ and C-Mad2−$Cdc20^{111-138}$ by gel filtration (data not shown). Furthermore, the absence of any free Mad1 peak from the gel filtration chromatogram suggested that the appearance of a C-Mad2−$Cdc20^{111-138}$ peak was not generated as an effect of competition by $Cdc20^{111-138}$ on the C-Mad2−$Mad1^{485-718}$ interaction.

We wanted to further confirm our data shown in Figure 3A by using a non-FP readout. C-Mad2−TRCdc20 formation was also determined by measuring the endogenous fluorescence (fluorescence intensity) of $TRCdc20^{111-138}$ bound to C-Mad2 at various time intervals after removing unbound $TRCdc20^{111-138}$ using desalting spin columns. Controls for this spin-column assay were as follows: (1) $TRCdc20^{111-138}$ (1 μM) alone represents our background fluorescence, (2) $TRCdc20^{111-138}$ (1 μM) incubated with unliganded C-Mad2 (1 μM) represents our maximum fluorescence signal at any given time relative to $TRCdc20^{111-138}$ alone, and (3) $TRCdc20^{111-138}$ (1 μM) incubated with C-Mad2−$Mad1^{485-718}$ (100 nM) shows that C-Mad2−$Mad1^{485-718}$ does contain loosely associated Mad2 molecules or that a $TRCdc20^{111-138}$ does not displace C-Mad2 from the C-Mad2−$Mad1^{485-718}$ core complex. To confirm C-Mad2−$Mad1^{485-718}$ catalysis of O-Mad2 using a non-FP assay, we incubated a 1:1 ratio of O-Mad2/ $TRCdc20^{111-138}$ (1 μM) in the presence and absence of a fixed amount of C-Mad2−$Mad1^{485-718}$ (100 nM) and measured the amount $TRCdc20^{111-138}$ bound to C-Mad2 by quantifying fluorescence intensity at various time intervals after desalting. The data generated from this time course experiment are shown in Figure 3C and confirm our kinetic FP results that a C-Mad2−$Mad1^{485-718}$ catalyzes the transformation of O-Mad2 into a Cdc20-bound C-Mad2 complex.

C-Mad2−Cdc20 Catalyzes O-Mad2 Binding to Cdc20. The main difference between the "Mad2 template" and "two-state" model is that the template model proposes that a newly formed C-Mad2−Cdc20 complex can promote its own transformation of O-Mad2 into Cdc20-bound C-Mad2. This aspect of

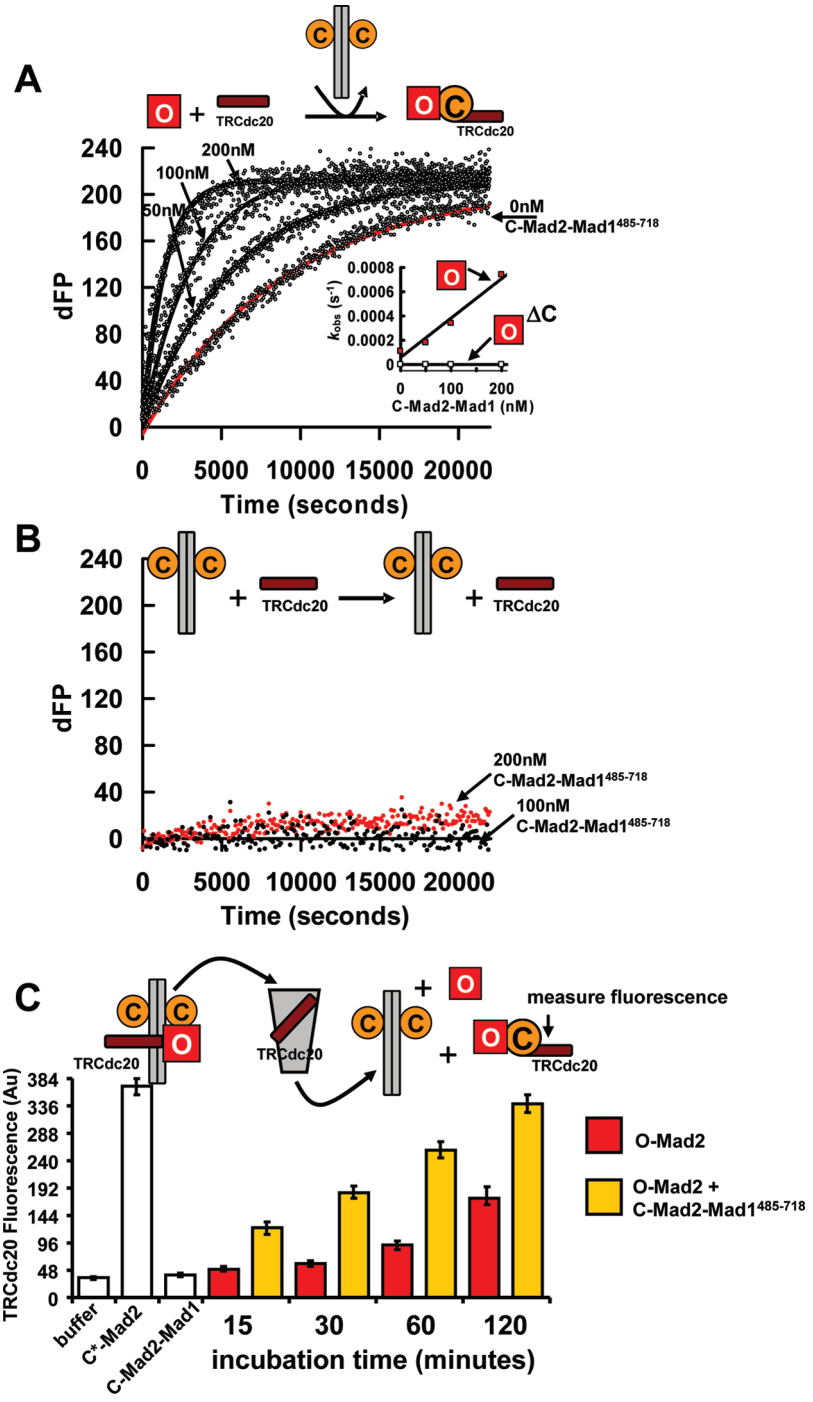

FIGURE 3: The C-Mad2−Mad1$^{485-718}$ core complex catalyzes the transformation of O-Mad2 into a C-Mad2−TRCdc20$^{111-138}$ complex. (A) Representative kinetic traces for a C-Mad2−Mad1$^{485-718}$ titration versus a fixed concentration of O-Mad2 (1 μM) and TRCdc20$^{111-138}$ (1 μM). The red line represents a single exponential fit for O-Mad2 only (0 nM Mad2−Mad1$^{485-718}$), and black lines represent a single exponential fit of the data in the presence of a C-Mad2−Mad1$^{485-718}$ core complex. Inset: First-order rate constants (k_{obs} (s^{-1})) for the catalyzed transformation of O-Mad2 into a C-Mad2−TRCdc20$^{111-138}$ complex plotted as a function of C-Mad2−Mad1$^{485-718}$ concentration (red squares) and Mad2$^{\Delta C}$ incubated with TRCdc20$^{111-138}$ as a function of C-Mad2−Mad1$^{485-718}$ (white squares). The data were fitted to a linear equation in order to determine the second-order rate constant. (B) Representative kinetic traces in the absence of O-Mad2 monitoring the binding between TRCdc20$^{111-138}$ (1 μM) and two concentrations of C-Mad2−Mad1$^{485-718}$ (200 and 100 nM). (C) Confirmation of C-Mad2−Mad1$^{485-718}$ catalysis of O-Mad2 into a C-Mad2−TRCdc20$^{111-138}$ complex using a non-FP readout. White bars represent the following experimental controls: buffer and TRCdc20$^{111-138}$ (1 μM); 1:1 ratio of C*-Mad2/TRCdc20$^{111-138}$ (1 μM) and TRCdc20$^{111-138}$ (1 μM) incubated with C-Mad2−Mad1$^{485-718}$ (100 nM). The colored bars represent a reaction time course between a 1:1 ratio of O-Mad2/TRCdc20$^{111-138}$ (1 μM) incubated in the absence (red bars) or presence (yellow bars) of a fixed concentration of the C-Mad2−Mad1$^{485-718}$ core complex (100 nM). TRCdc20$^{111-138}$ fluorescence was determined after spin column desalting and represents C-Mad2−TRCdc20$^{111-138}$ complex formation at the various indicated time intervals.

the template model, which is based on the structural similarity of the C-Mad2−Cdc20 and C-Mad2−Mad1 complexes, is still unresolved since both biochemical and mathematical stimulations have come to conflicting conclusions (*29*−*31*, *33*). We wanted to directly test this aspect of the Mad2 template using our assay. We acknowledge that a possible caveat with our

experiment is that we are not using full-length human Cdc20, which is a larger protein than Mad2 itself (~55 kDa compared to ~25 kDa). As a consequence, we recognize that the binding of a 55 kDa protein compared to a 28 amino acid fragment to Mad2 could be different.

To determine if a C-Mad2 bound to a small fragment of Cdc20 has the catalytic capability to transform O-Mad2 into C-Mad2, we first preformed a C-Mad2−Cdc20$^{111-138}$ complex by incubating O-Mad2 with ~30-fold excess of unlabeled Cdc20$^{111-138}$ overnight (~12 h) at room temperature. Excess Cdc20$^{111-138}$ was removed by gel filtration, and the elution profile from a Superdex-200 size-exclusion chromatography column revealed that in the presence of superstoichiometric Cdc20$^{111-138}$ the C-Mad2−Cdc20$^{111-138}$ complex elutes as a monomer (Figure 4A). Our SEC elution profiles for Mad2 in the presence of stoichiometric and superstoichiometric amounts of Cdc20$^{111-138}$ are consistent with previously published data (*41*) and indicate that the oligomeric state of Mad2 is sensitive to Cdc20 concentration. We then assessed the catalytic capability of our preformed C-Mad2−Cdc20$^{111-138}$ complex by kinetically monitoring the binding between O-Mad2 (1 μM) and TRCdc20$^{111-138}$ (1 μM) in the presence of catalytic concentrations of C-Mad2−Cdc20$^{111-138}$ (0−200 nM). Figure 4B shows representative traces for O-Mad2 binding to TRCdc20$^{111-138}$ in the presence of C-Mad2−Cdc20$^{111-138}$. Under these experimental conditions we are able to directly show for the first time that a C-Mad2−Cdc20 complex (C-Mad2−Cdc20$^{111-138}$) has the catalytic capability to transform O-Mad2 into a Cdc20-bound C-Mad2 complex.

The observed rates for the formation of a C-Mad2−TRCdc20$^{111-138}$ complex (k_{obs}) showed a linear dependence upon C-Mad2−Cdc20$^{111-138}$ concentration between 0 and 200 nM (Figure 4B, inset) and yielded a second-order rate constant of 2.2×10^{-3} μM s^{-1} which is comparable to that determined for the C-Mad2−Mad1$^{485-718}$-catalyzed reaction (Table 2). However, when we monitored the reaction between C-Mad2−Cdc20$^{111-138}$ (0−200 nM) and TRCdc20$^{111-138}$ (1 μM) in the absence of O-Mad2, we observed relatively small but slower increases in FP compared to the O-Mad2-catalyzed reaction (Figure 4C). The slow increase in FP indicates the formation of the C-Mad2−TRCdc20$^{111-138}$ complex and most likely was caused by TRCdc20$^{111-138}$ competing with unlabeled Cdc20$^{111-138}$ bound to C-Mad2. We do not anticipate the competition between labeled and unlabeled Cdc20$^{111-138}$ to influence the catalyzed reaction because it occurs significantly more slowly than the catalysis of O-Mad2 into Cdc20$^{111-138}$-bound C-Mad2 (Figure 4B,C). More importantly, the availability of "free" TRCdc20$^{111-138}$ to compete with unlabeled Cdc20$^{111-138}$ bound to C-Mad2 would be significantly smaller in a catalyzed reaction (presence of O-Mad2) because it would be depleted by the binding to the catalytically transformed O-Mad2. We conducted similar experiments using a preformed O−C Mad2−Cdc20$^{111-138}$ complex (1:1 incubation of Mad2 with an equimolar concentration of Cdc20$^{111-138}$) and found that it also induced catalytic transformation of O-Mad2 into a C-Mad2−TRCdc20$^{111-138}$ complex. However, when we monitored the reaction between O−C Mad2−Cdc20$^{111-138}$ and TRCdc20$^{111-138}$ in the absence of O-Mad2, we observed a larger increase in FP signal compared to the equivalent C-Mad2−Cdc20$^{111-138}$ reaction. The larger increase in FP signal, which occurs on a similar time scale to the basal binding reaction between O-Mad2 and TRCdc20$^{111-138}$, is caused by the extra

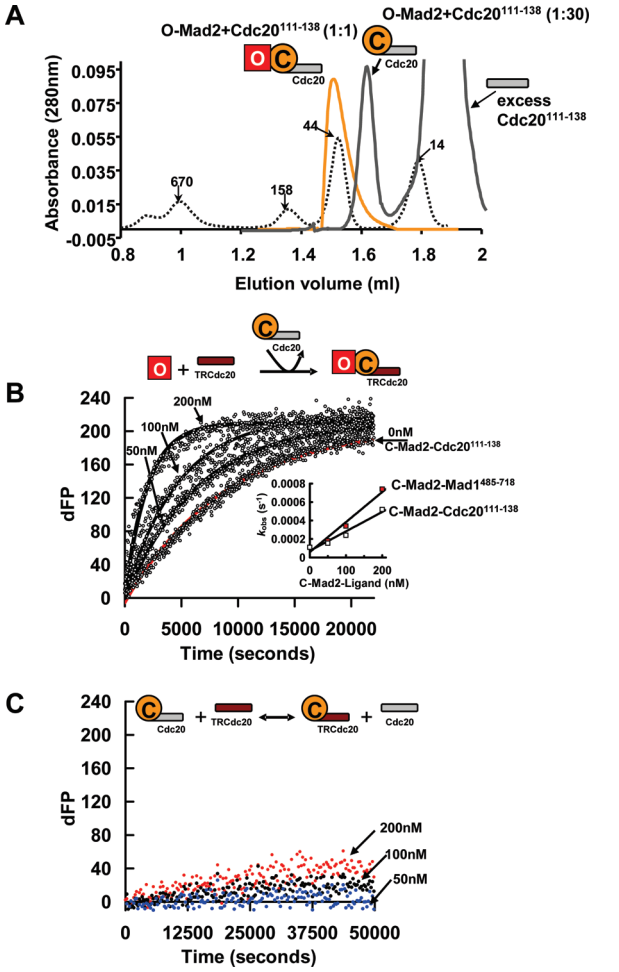

FIGURE 4: The preformed C-Mad2−Cdc20$^{111-138}$ complex catalyzes its own transformation of O-Mad2 into a C-Mad2−TRCdc20$^{111-138}$ complex. (A) Elution profiles of O-Mad2 incubated in the presence of stoichiometric and superstoichiometric amounts of Cdc20$^{111-138}$ from a Superdex-200 PC 3.2/30 column monitored at A_{280nm}. O-Mad2 incubated in the presence of an equimolar amount of Cdc20$^{111-138}$ elutes as a dimer (yellow line) whereas O-Mad2 incubated in the presence of a 30-fold excess of Cdc20$^{111-138}$ elutes as a monomer (gray line). Molecular weight markers are represented as a black dotted line. The final protein concentration for O-Mad2 incubated with Cdc20$^{111-138}$ was 4 μM. (B) Representative kinetic traces for a C-Mad2−Cdc20$^{111-138}$ titration versus a fixed concentration of O-Mad2 (1 μM) and TRCdc20$^{111-138}$ (1 μM). The red line represents a single exponential fit for O-Mad2 only (0 nM C-Mad2−Cdc20$^{111-138}$), and black lines represent a single exponential fit of the data in the presence of C-Mad2−Cdc20$^{111-138}$. Inset: First-order rate constants (k_{obs} (s^{-1})) for the transformation of O-Mad2 into a C-Mad2−TRCdc20$^{111-138}$ complex plotted as a function of either C-Mad2−Mad1$^{485-718}$ (red squares) or C-Mad2−Cdc20$^{111-138}$ (white squares). The data were fitted to a linear equation in order to obtain a second-order rate constant. (C) Representative kinetic traces in the absence of O-Mad2 monitoring the binding between TRCdc20$^{111-138}$ (1 μM) and various concentrations of C-Mad2−Cdc20$^{111-138}$.

Mad2 molecule binding to TR-Cdc20$^{111-138}$ (Supporting Information Figure S3).

Kinetic Analysis of Mad2$^{R133E-Q134A}$. So far, (1) we have shown that the basal rate for the interaction between O-Mad2 and TRCdc20$^{111-138}$ is ~300-fold slower than unliganded C-Mad2, (2) we have confirmed that a C-Mad2−Mad1$^{485-718}$ core complex catalyzes the transformation of O-Mad2 into Cdc20-bound C-Mad2, and (3) we have shown that a preformed C-Mad2−Cdc20$^{111-138}$ complex has catalytic properties similar

Table 2: Kinetic Constants for C-Mad2−TRCdc20$^{111-138}$ Formation

constants	protein	
K_d for C-Mad−TRCdc20$^{111-138}$	wild type (μM)[a]	0.16 ± 0.04
	wild type (μM)	0.17 ± 0.04
	mutant (μM)	0.26 ± 0.04
reactions: Mad2 (1 μM) + TRCdc20$^{111-138}$ (1 μM)		
basal binding for O-Mad2	wild type (s^{-1})	0.00012
	mutant (s^{-1})	0.000043
basal binding for C*-Mad2	wild type (s^{-1})	0.037
	mutant (s^{-1})	0.030
C-Mad2−Mad1$^{485-718}$ catalysis	wild-type O-Mad2 ($\mu M\ s^{-1}$)	3.3×10^{-3}
C-Mad2−Cdc20$^{111-138}$ catalysis	wild-type O-Mad2 ($\mu M\ s^{-1}$)	2.2×10^{-3}

[a]Determined by ITC.

to those of a core C-Mad2−Mad1 complex and therefore is able to promote its own transformation of O-Mad2. This later observation would have influenced the basal rate for the interaction between O-Mad2 and TRCdc20$^{111-138}$. In order to determine a basal rate for the interaction between O-Mad2 and TRCdc20$^{111-138}$ that was not influenced by Mad2 conformational dimerization (the ability to form O−C Mad2), we kinetically characterized a Mad2 mutant that was impaired in its ability to form O−C Mad2 but retains the ability to bind Cdc20. The Mad2$^{R133E-Q134A}$ double mutant (for simplicity the Mad2 double mutant will now on be referred to as Mad2^{RQ}) has been shown to exclusively exist as a monomer, retains the ability to bind Cdc20, but failed to bind C-Mad2−Mad1 (Table 1).

We separated and isolated both O-Mad2^{RQ} and unliganded C-Mad2^{RQ} conformers using anion-exchange chromatography. Using analytical gel filtration we confirmed previously published reports that both O-Mad2^{RQ} and unliganded C-Mad2^{RQ} conformers exist as monomers (Figure 5A). Using our Mad2 FP assay we found that unliganded C-Mad2^{RQ} and wild-type Mad2 bind TRCdc20$^{111-138}$ with similar affinity ($K_{d,Mad2\text{-}RQ}$ = 0.26 μM, and $K_{d,Mad2}$ = 0.17 μM, respectively). Surprisingly, we observed ~50% drop in the FP signal for the formation C-Mad2^{RQ}−TRCdc20$^{111-138}$ compared to the wild-type protein (Figure 5B). This difference in FP amplitude was also observed when we determined the basal binding rate between O-Mad2^{RQ} (1 μM) and TRCdc20$^{111-138}$ (1 μM) (Figure 5C). The ~50% reduction in amplitude observed for the formation of a C-Mad2^{RQ}-TRCdc20$^{111-138}$ complex compared to the wild-type protein is consistent with Mad2^{RQ} exclusively existing as a monomer and complements the SEC data for Mad2^{RQ}. The basal rate for the transformation of O-Mad2 into a C-Mad2−TRCdc20$^{111-138}$ complex was ~4-fold slower for Mad2^{RQ} (k_{obs} = 0.000043 s^{-1}) compared to the wild-type protein (k_{obs} = 0.00012 s^{-1}). On the other hand, the basal binding rate between unliganded C-Mad2^{RQ} and TRCdc20$^{111-138}$ was comparable to the equivalent wild-type reaction (Table 2). To corroborate the Mad2^{RQ} time-dependent FP signal, we measured the binding between TRCdc20$^{111-138}$ and Mad2$^{RQ\text{-}\Delta C}$ (Figure 5C). Mad2$^{RQ\text{-}\Delta C}$ is a Mad2$^{R133E-Q134A}$ double mutant that is unable to bind Mad1 or Cdc20 because a 10-residue C-terminal deletion locks the safety belt in the O-Mad2 conformation (Table 1). Incubation of Mad2$^{RQ\text{-}\Delta C}$ with TRCdc20$^{111-138}$ did not produce a time-dependent FP signal change (Figure 5C), confirming that Mad2$^{RQ\text{-}\Delta C}$ cannot bind Cdc20 and also that the time-dependent increase in FP signal observed between O-Mad2^{RQ} and TRCdc20$^{111-138}$ represents C-Mad2^{RQ}−TRCdc20$^{111-138}$ complex formation.

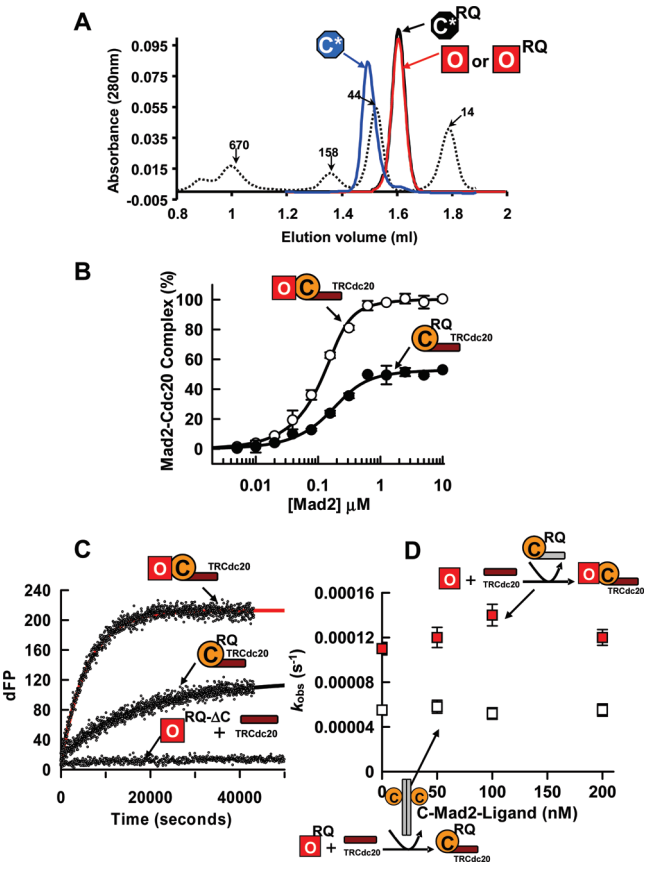

FIGURE 5: Kinetic analysis of Mad2^{RQ}. (A) SEC elution profiles of wild type and Mad2^{RQ} conformers from a Superdex-200 PC 3.2/30 column were monitored at A_{280nm}. C*-Mad2 (blue line); C*-Mad2^{RQ} (black line); red line represents both O-Mad2 and O-Mad2^{RQ}. Molecular weight markers are represented as a black dotted line. Final protein concentrations for Mad2 were 4 μM. (B) Equilibrium binding of TRCdc20$^{111-138}$ to either C*-Mad2 or C*-Mad2^{RQ} in an FP assay. The equilibrium dissociation constant was measured by titrating Mad2 at a fixed concentration of TRCdc20$^{111-138}$ (75 nM). The binding data (mP) were transformed and fit to a quadratic equation. (C) Kinetic traces comparing the transformation of either O-Mad2 or O-Mad2^{RQ} into a TRCdc20$^{111-138}$-bound C-Mad2 or C-Mad2^{RQ} complex, respectively. As a control, a kinetic trace for the reaction between Mad2$^{RQ\text{-}\Delta C}$ and TRCdc20$^{111-138}$ is shown. Protein concentrations for the kinetic reactions were 1 μM Mad2 and 1 μM TRCdc20$^{111-138}$. Kinetic traces were fit to a single exponential equation (red line for O-Mad2 and black line for O-Mad2^{RQ}) in order to obtain a first-order rate constant. (D) Rate constants for the formation of either C-Mad2−TRCdc20$^{111-138}$ or C-Mad2^{RQ}−TRCdc20$^{111-138}$ catalyzed by either C-Mad2^{RQ}−Cdc20$^{111-138}$ (red squares) or C-Mad2−Mad1$^{485-718}$ (white squares), respectively.

Another notable difference between O-Mad2^{RQ} and the wild-type protein was the absence of an initial lag phase at low Mad2 concentrations during the formation of C-Mad2−TRCdc20$^{111-138}$. The lag phase and subsequent sigmoidal kinetic trace, which would be typical for an autocatalytic reaction, were only observed during the basal wild-type O-Mad2 reaction (Figure 2D). We postulate that the initial lag phase represents the slow accumulation of C-Mad2−TRCdc20$^{111-138}$, which is followed by a faster reaction as a result of C-Mad2−TRCdc20$^{111-138}$ catalysis. Mad2^{RQ} is unable to form O−C Mad2 and therefore should not give rise to an autocatalytic reaction whereby C-Mad2^{RQ}−TRCdc20$^{111-138}$ induces its own synthesis. The absence of the lag phase and overall slower rate of C-Mad2−TRCdc20$^{111-138}$ formation for Mad2^{RQ} compared to the wild-type protein suggest that the rate of TRCdc20$^{111-138}$ binding to Mad2^{RQ} represents the actual basal rate of Mad2 binding to TRCdc20$^{111-138}$ in the absence of Mad2 conformational dimerization.

To further highlight the importance of Mad2 conformational dimerization for C-Mad2−Cdc20 formation, we kinetically monitored the binding between O-Mad2 (1 μM) and TRCdc20$^{111-138}$ (1 μM) in the presence of a preformed C-Mad2^{RQ}−Cdc20$^{111-138}$ complex (0−200 nM). To complement this experiment, we also measured the binding kinetics between O-Mad2^{RQ} (1 μM) and TRCdc20$^{111-138}$ (1 μM) in the presence of C-Mad2−Mad1$^{485-718}$ (0−200 nM). If conformational dimerization of Mad2 is required to catalytically transform O-Mad2 into a C-Mad2−Cdc20 complex, then O-Mad2^{RQ} should be insensitive to C-Mad2−Mad1$^{485-718}$ catalysis whereas a preformed C-Mad2^{RQ}−Cdc20$^{111-138}$ complex should not be able to catalyze the transformation of wild-type O-Mad2 into a C-Mad2−TRCdc20$^{111-138}$ complex. The data for these experiments are shown in Figure 5D and reveal that the rate of either O-Mad2^{RQ} or wild-type O-Mad2 transformation into a Cdc20-bound C-Mad2 complex cannot be catalyzed by either a core C-Mad2−Mad1$^{485-718}$ or a preformed C-Mad2^{RQ}−Cdc20$^{111-138}$ complex, respectively. These data are consistent with a recently published SEC experiment which showed that a C-Mad2^{RQ}–Mad1$^{485-718}$ complex was unable to convert O-Mad2 into C-Mad2 in the absence of Cdc20 (*27*).

DISCUSSION

In this present study we have used a novel in vitro homogeneous Mad2 activity assay to define the molecular basis for C-Mad2−Cdc20 formation. Using our assay we were able to directly measure the basal binding rate for both O-Mad2 and unliganded C-Mad2 with TRCd20$^{111-138}$ and found that O-Mad2 binds TRCdc20$^{111-138}$ ~300 fold more slowly than unliganded C-Mad2 (Table 2). The ability of our assay to be able to distinguish between O-Mad2 and unliganded C-Mad2 indicates that it can also serve as a real time sensor for Mad2 conformation. The slow binding of O-Mad2 to TRCdc20$^{111-138}$ provides an explanation for previously published data showing that unliganded C-Mad2 is more active than O-Mad2 in APC/C^{Cdc20} inhibition in vitro (*10*). This is because the difference in their APC/C^{Cdc20} inhibitory activity is due to significantly different binding rates to Cdc20. An important goal of this study was to confirm recently published work demonstrating the catalytic properties of C-Mad2−Mad1 on the transformation of O-Mad2 into a C-Mad2−Cdc20 complex (*27*, *29*, *30*). Surprisingly, although we were able to demonstrate that a stable C-Mad2−Mad1$^{485-718}$ core complex was able to accelerate the binding between O-Mad2 and TRCdc20$^{111-138}$, we did not observe C-Mad2−Mad1 catalysis for the binding between unliganded C-Mad2 and TRCdc20$^{111-138}$. These data combined with the basal Mad2 binding data suggest that asymmetric conformational dimerization of Mad2 (formation of O−C Mad2) is required for O-Mad2 catalysis and that the binding between O-Mad2 and Cdc20 is rate-limiting for the formation of a C-Mad2−Cdc20 complex. These assumptions are consistent with recent crystallographic data which revealed an asymmetric interface that explains the selective dimerization of O-Mad2 onto a C-Mad2−ligand complex (*18*, *27*).

A fundamental difference between the "Mad2 template" and "two-state" models for Mad2 activation is the contribution of an autocatalytic loop that is thought to propagate and amplify C-Mad2−Cdc20 formation (*20*). The Mad2 "template" model proposes that a C-Mad2−Cdc20 complex might be endowed with the same catalytic properties as the C-Mad2−Mad1 complex. This aspect of the "template" model, which is based on the structural similarity of the C-Mad2−Cdc20 and C-Mad2−Mad1 complexes, is currently under debate (*29*−*31*, *33*). Using our Mad2 FP assay we were able to directly demonstrate for the first time that a preformed C-Mad2−Cdc20$^{111-138}$ complex can catalyze the transformation of O-Mad2 into a C-Mad2−TRCdc20$^{111-138}$ complex independent of C-Mad2−Mad1. Although the use of a small fragment of Cdc20 (Cdc20$^{111-138}$ peptide) is clearly not mimicking a physiological situation, it is revealing in the sense that it shows us the minimum Mad2 scaffold required to recruit and catalytically transform O-Mad2 into a C-Mad2−Cdc20 complex. We also recognize that the use of the Cdc20 peptide rather than the full-length protein may not reveal the entire story; in particular, the fact that Cdc20$^{111-138}$ is a stronger Mad2 ligand than the full-length protein (*35*, *36*) would suggest additional destabilizing interactions may take place between Mad2 and full-length Cdc20. We suspect that full-length Cdc20 would affect the rate at which C-Mad2−Cdc20 is formed and destabilized.

Characterizing the kinetics of C-Mad2−Cdc20 formation by using a Mad2 mutant that was impaired in its ability to form O−C Mad2 but retained the ability to bind Cdc20 confirmed the catalytic capabilities of a C-Mad2−ligand complex and, at the same time, provided additional insights into the mechanism of C-Mad2−Cdc20 formation. Equilibrium binding experiments and SEC elution profiles for Mad2^{RQ} confirmed that the mutant protein exclusively exists as a monomer (unable to bind a second Mad2 molecule) and that the mutations did not impair its ability to bind Cdc20. These data are consistent with previous work (*18*, *20*) and make sense when considering that residues R133 and Q134 are localized at the interface between O-Mad2 and C-Mad2 and that the dimerization interface occupies the opposite end of Mad2 from where Cdc20 binds. The inability of O-Mad2^{RQ} to be catalyzed by a C-Mad2−Mad1$^{485-718}$ complex or a C-Mad2^{RQ}–Cdc20$^{111-138}$ complex to catalyze wild-type O-Mad2 is consistent with a catalytic model in which conformational dimerization of Mad2 is coupled to a catalytic activity that primes Mad2 for Cdc20 binding. Comparison of the basal rates of C-Mad2−TRCdc20$^{111-138}$ formation for wild type and Mad2^{RQ} enabled us to determine the actual basal rate of Mad2 binding to TRCdc20$^{111-138}$ but also provided further support that asymmetric conformational dimerization of Mad2 (O-Mad2 recruited by C-Mad2 to form O−C Mad2) and not symmetric conformational dimerization (unliganded C-Mad2 recruited by C-Mad2 to form C−C Mad2) accelerates the formation of a

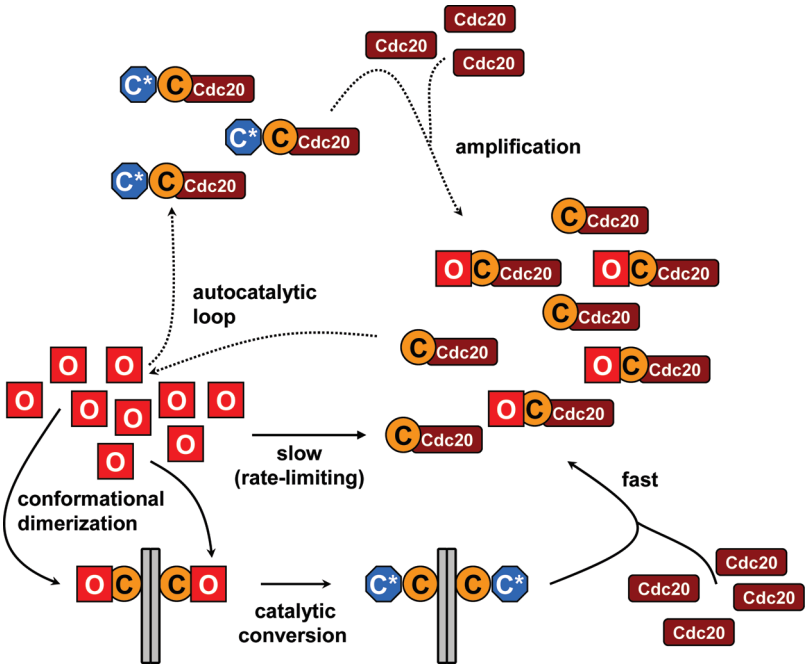

FIGURE 6: Kinetic model summarizing the biochemical mechanism for C-Mad2−Cdc20 formation. In the absence of C-Mad2−Mad1 or C-Mad2−Cdc20 the rate-limiting step for the formation of C-Mad2−Cdc20 is the transformation of O-Mad2 into C*-Mad2. Conformational dimerization of O-Mad2 onto C-Mad2−Mad1 accelerates the conversion of O-Mad2 into C*-Mad2 which then dissociates and rapidly binds Cdc20. The newly formed C-Mad2−Cdc20 complex is able to promote its own transformation of O-Mad2 into C-Mad2−Cdc20 independent of C-Mad2−Mad1 through an autocatalytic loop (dashed arrows). The autocatalytic loop, initially proposed for the "Mad2 template" model, propagates the amplification of C-Mad2−Cdc20.

C-Mad2−Cdc20 complex. We observed a 4-fold difference in the basal binding rates for C-Mad2−TRCdc20$^{111-138}$ formation between wild-type O-Mad2 and O-Mad2^{RQ}, whereas the binding rates of unliganded C-Mad2 and unliganded C-Mad2^{RQ} to TRCdc20$^{111-138}$ were comparable (Table 2). Interestingly, the kinetic comparison of C-Mad2−TRCdc20$^{111-138}$ formation between Mad2^{RQ} and the wild type also revealed that wild-type O-Mad2, which exists as a monomer in the absence of Cdc20, converts into a dimer during TRCdc20$^{111-138}$ binding. This observation is consistent with recently published SEC data which showed that incubation of O-Mad2 with a stable C-Mad2−Mad1$^{485-718}$ core complex in the absence of Cdc20 promoted the formation of unliganded C-Mad2 (*27*). The SEC data combined with our wild-type and Mad2^{RQ} kinetic data, which also includes that a C-Mad2−Mad1$^{485-718}$ complex was unable to catalyze the binding between unliganded C-Mad2 and TRCdc20$^{111-138}$, provide strong support that conformational dimerization of O-Mad2 onto a C-Mad2−ligand complex generates unliganded C-Mad2 which then rapidly binds TRCdc20$^{111-138}$.

In cells it is estimated that the checkpoint is fully active in approximately 12 min after nuclear envelope breakdown (*42*). Published cellular concentrations of Mad2 and Cdc20 reveal that they are present in approximately equimolar concentrations (~120 nM for Mad2 and ~100 nM for Cdc20) (*29*). The cellular concentration of C-Mad2−Mad1 has been estimated to be one-tenth the concentration of Mad2 and Cdc20 (~10 nM) (*30*). This estimation was based on the assumption that approximately 1000 C-Mad1−Mad1 molecules bind at each unattached kinetochore in a cell which contains ~22 kinetochores, all of which are unattached at the beginning of prometaphase and therefore all contribute to checkpoint activation (*30*). Our in vitro experiments measuring C-Mad2−Cdc20 formation using comparable cellular protein ratios of Mad2, Cdc20, and C-Mad2−Mad1 (Figure 3A) reveal that the time scale of C-Mad2−Cdc20 formation is significantly slower (~4 h) compared to the time scale of spindle checkpoint establishment in cells (~12 min). An obvious possible explanation for the disagreement between our in vitro data and cellular observations is the underestimation of C-Mad2−Mad1 concentration at unattached kinetochores. Our in vitro data reveal that an 8-fold increase in C-Mad2−Mad1$^{485-718}$ concentration reduces the time scale of C-Mad2−Cdc20$^{111-138}$ formation to approximately ~19 min (Supporting Information Figure S4). Another reason for the discrepancy might be that our in vitro measurements do not contain additional factors needed to accelerate the binding between O-Mad2 and Cdc20 in vivo. For instance, in our in vitro experiments we only use the Mad2 binding domains of Mad1 (residues 485−178) and Cdc20. The inclusion of full-length Mad1 may structurally alter the C-Mad2 dimer interface which may increase the association, catalytic transformation, and dissociation of a second Mad2. Phosphorylation of Cdc20, which cannot be achieved in our in vitro experiments, may also provide an additional factor for accelerating conformational dimerization.

During the preparation of this report Simonetta and coworkers published work analyzing the catalytic conversions of O-Mad2 to C-Mad2 using both quantitative imaging-based binding assays and computational simulations (*30*). Using both wild type and a Mad2 mutant that could not dimerize but retained the ability to bind Cdc20 (Mad2^{F141A}), they demonstrated catalytic conversion of O-Mad2 to C-Mad2 by both C-Mad2−Mad1 and C-Mad2−Cdc20$^{111-138}$. They reported similar observations and comparable rate constants to those generated using our Mad2 FP assay; however, a kinetic characterization for the binding between unliganded C-Mad2 and Cdc20 was not reported (*30*). Our ability to characterize the binding of both O-Mad2 and unliganded C-Mad2 to Cdc20$^{111-138}$ has enabled us to support and confirm previously reported data but, at the same time, provide additional mechanistic insights for the

steps that accelerate the transformation of Mad2 into a C-Mad2−Cdc20 complex. In summary, our results show O-Mad2 has to overcome a large kinetic barrier in order to bind Cdc20. Asymmetric conformational dimerization of O-Mad2 onto a C-Mad2−Mad1 core complex converts O-Mad2 into a kinetically favorable conformation that can directly bind Cdc20 to form C-Mad2−Cdc20 (Figure 6). We also show that asymmetric conformational dimerization of O-Mad2 onto either C-Mad2−Mad1 or C-Mad2−Cdc20 generates unliganded C-Mad2 which then dissociates to bind Cdc20. Using $Cdc20^{111-138}$ we have attempted to provide direct experimental support for the "Mad2 template" model in which a newly formed C-Mad2−Cdc20 complex generates an autocatalytic loop that propagates the amplification of C-Mad2−Cdc20 independent of C-Mad2−Mad1. Lastly, our unique Mad2 assay provides a readout to perform direct in vitro studies of other components of SAC and screening for small molecule drug-like compounds that modulate this key biological process.

ACKNOWLEDGMENT

We thank Donglin Guo, Dr. Ramesh Baliga, Dr. Daniel Pierce, Leah Lad, Hung Tran, and Dr. Katjusa Brejc for support, encouragement, and critical advice during the preparation of the manuscript.

SUPPORTING INFORMATION AVAILABLE

Kinetic traces for an O-Mad2 titration versus $TRCdc20^{111-138}$ (Figure S1), the binding between $TRCdc20^{111-138}$ and C*-Mad2 ± C-Mad2−Mad1 (Figure S2), the reaction between O−C Mad2−$Cdc20^{111-138}$ and $TRCdc20^{111-138}$ (Figure S3), and the kinetic traces for a C-Mad2−$Mad1^{485-718}$ titration (0−800 nM) versus a fixed concentration of O-Mad2 (1 μM) and $TRCdc20^{111-138}$ (1 μM) (Figure S4). This material is available free of charge via the Internet at http://pubs.acs.org.

REFERENCES

1. Musacchio, A., and Hardwick, K. G. (2002) The spindle checkpoint: structural insights into dynamic signalling. *Nat. Rev. Mol. Cell Biol. 3*, 731–741.
2. Weaver, B. A., and Cleveland, D. W. (2005) Decoding the links between mitosis, cancer, and chemotherapy: the mitotic checkpoint, adaptation, and cell death. *Cancer Cell 8*, 7–12.
3. Bharadwaj, R., and Yu, H. (2004) The spindle checkpoint, aneuploidy, and cancer. *Oncogene 23*, 2016–2027.
4. Peters, J. M. (2006) The anaphase promoting complex/cyclosome: a machine designed to destroy. *Nat. Rev. Mol. Cell Biol. 7*, 644–656.
5. Hwang, L. H., Lau, L. F., Smith, D. L., Mistrot, C. A., Hardwick, K. G., Hwang, E. S., Amon, A., and Murray, A. W. (1998) Budding yeast Cdc20: a target of the spindle checkpoint. *Science 279*, 1041–1044.
6. Kim, S. H., Lin, D. P., Matsumoto, S., Kitazono, A., and Matsumoto, T. (1998) Fission yeast Slp1: an effector of the Mad2-dependent spindle checkpoint. *Science 279*, 1045–1047.
7. Howell, B. J., Hoffman, D. B., Fang, G., Murray, A. W., and Salmon, E. D. (2000) Visualization of Mad2 dynamics at kinetochores, along spindle fibers, and at spindle poles in living cells. *J. Cell Biol. 150*, 1233–1250.
8. Howell, B. J., Moree, B., Farrar, E. M., Stewart, S., Fang, G., and Salmon, E. D. (2004) Spindle checkpoint protein dynamics at kinetochores in living cells. *Curr. Biol. 14*, 953–964.
9. Shah, J. V., Botvinick, E., Bonday, Z., Furnari, F., Berns, M., and Cleveland, D. W. (2004) Dynamics of centromere and kinetochore proteins; implications for checkpoint signaling and silencing. *Curr. Biol. 14*, 942–952.
10. Fang, G., Yu, H., and Kirschner, M. W. (1998) The checkpoint protein MAD2 and the mitotic regulator CDC20 form a ternary complex with the anaphase-promoting complex to control anaphase initiation. *Genes Dev. 12*, 1871–1883.
11. Kallio, M., Weinstein, J., Daum, J. R., Burke, D. J., and Gorbsky, G. J. (1998) Mammalian p55CDC mediates association of the spindle checkpoint protein Mad2 with the cyclosome/anaphase-promoting complex, and is involved in regulating anaphase onset and late mitotic events. *J. Cell Biol. 141*, 1393–1406.
12. Wassmann, K., and Benezra, R. (2003) Mad2 transiently associates with an APC/p55Cdc complex during mitosis. *Proc. Natl. Acad. Sci. U.S.A. 95*, 11193–11198.
13. Chen, R. H., Shevchenko, A., Mann, M., and Murray, A. W. (1998) Spindle checkpoint protein Xmad1 recruits Xmad2 to unattached kinetochores. *J. Cell Biol. 143*, 283–295.
14. Chung, E., and Chen, R. H. (2002) Spindle checkpoint requires Mad1-bound and Mad1-free Mad2. *Mol. Biol. Cell 13*, 1501–1511.
15. Luo, X., Tang, Z., Rizo, J., and Yu, H. (2002) The Mad2 spindle checkpoint protein undergoes similar major conformational changes upon binding to either Mad1 or Cdc20. *Mol. Cell 9*, 59–71.
16. Luo, X., Fang, G., Coldiron, M., Lin, Y., Yu, H., Kirschner, M. W., and Wagner, G. (2000) Structure of the Mad2 spindle assembly checkpoint protein and its interaction with Cdc20. *Nat. Struct. Biol. 7*, 224–229.
17. Luo, X., Tang, Z., Xia, G., Wassmann, K., Matsumoto, T., Rizo, J., and Yu, H. (2004) The Mad2 spindle checkpoint protein has two distinct natively folded states. *Nat. Struct. Mol. Biol. 11*, 338–345.
18. Mapelli, M., Massimiliano, L., Santaguida, S., and Musacchio, A. (2007) The Mad2 conformational dimer: structure and implications for the spindle assembly checkpoint. *Cell 131*, 730–743.
19. Sironi, L., Mapelli, M., Knapp, S., De Antoni, A., Jeang, K., and Musacchio, A. (2002) Crystal structure of the tetrameric Mad1-Mad2 core complex: implications of a "safety belt" binding mechanism for the spindle checkpoint. *EMBO J. 21*, 2496–2506.
20. De Antoni, A., Pearson, C. G., Cimini, D., Canman, J. C., Sala, V., Nezi, L., Mapelli, M., Sironi, L., Faretta, M., Salmon, E. D., and Musacchio, A. (2005) The Mad1/Mad2 complex as a template for Mad2 activation in the spindle assembly checkpoint. *Curr. Biol. 15*, 214–225.
21. Lenart, P., and Peters, J. M. (2006) Checkpoint activation: don't get mad too much. *Curr. Biol. 16*, R412–R414.
22. Mapelli, M., and Musacchio, A. (2007) MAD contortions: conformational dimerization boosts spindle checkpoint signaling. *Curr. Opin. Struct. Biol. 17*, 716–725.
23. Musacchio, A., and Salmon, E. D. (2007) The spindle-assembly checkpoint in space and time. *Nat. Rev. Mol. Cell Biol. 8*, 379–393.
24. Nasmyth, K. (2005) How do so few control so many? *Cell 120*, 739–746.
25. Peters, J. M. (2008) Checkpoint control: the journey continues. *Curr. Biol. 18*, R170–R172.
26. Yu, H. (2006) Structural activation of Mad2 in the mitotic spindle checkpoint: the two-state Mad2 model versus the Mad2 template model. *J. Cell Biol. 173*, 153–157.
27. Yang, M., Li, B., Liu, C., Tomchick, D. R., Machius, M., Rizo, J., Yu, H., and Luo, X. (2008) Insights into Mad2 regulation in the spindle checkpoint revealed by the crystal structure of the symmetric Mad2 dimer. *PLoS Biol. 6*, 1–13.
28. Vink, M., Simonetta, M., Transidico, P., Ferrari, K., Mapelli, M., De Antoni, A., Massimiliano, L., Ciliberto, A., Faretta, M., Salmon, E. D., and Musacchio, A. (2006) In vitro FRAP identifies the minimal requirements for Mad2 kinetochore dynamics. *Curr. Biol. 16*, 755–766.
29. Kulukian, A., Han, J. S., and Cleveland, D. W. (2009) Unattached kinetochores catalyze production of an anaphase inhibitor that requires a Mad2 template to prime Cdc20 for BubR1 binding. *Dev. Cell 16*, 105–117.
30. Simonetta, M., Manzoni, R., Mosca, R., Mapelli, M., Massimiliano, L., Vink, M., Novak, B., Musacchio, A., and Ciliberto, A. (2009) The influence of catalysis on Mad2 activation dynamics. *PLoS Biol. 7*, 1–14.
31. Doncic, A., Ben-Jacob, E., and Barkai, N. (2005) Evaluating putative mechanisms of the mitotic spindle checkpoint. *Proc. Natl. Acad. Sci. U.S.A. 102*, 6332–6337.
32. Sear, R. P., and Howard, M. (2006) Modeling dual pathways for the metazoan spindle assembly checkpoint. *Proc. Natl. Acad. Sci. U.S.A. 103*, 16758–16763.
33. Ibrahim, B., Dittrich, P., Diekmann, S., and Schmitt, E. (2008) Mad2 binding is not sufficient for complete Cdc20 sequestering in mitotic transition control (an in silico study). *Biophys. Chem. 134*, 93–100.
34. Heyduk, T., Ma, Y., Tang, H., and Ebright, R. H. (1996) Fluorescence anisotropy: rapid, quantitative assay for protein-DNA and protein-protein interaction. *Methods Enzymol. 274*, 492–503.

35. Tang, Z., Bharadwaj, R., Li, B., and Yu, H. (2001) Mad2-independent inhibition of APCCdc20 by the mitotic checkpoint protein BubR1. *Dev. Cell 1*, 227–237.
36. Zhang, Y., and Lees, E. (2001) Identification of an overlapping binding domain on Cdc20 for Mad2 and anaphase-promoting complex: model for spindle checkpoint regulation. *Mol. Cell. Biol. 21*, 5190–5199.
37. Sironi, L., Melixetian, M., Faretta, M., Prosperini, E., Helin, K., and Musacchio, A. (2001) Mad2 binding to Mad1 and Cdc20, rather than oligomerization, is required for the spindle checkpoint. *EMBO J. 20*, 6371–6382.
38. Copeland, R. A. (2000) Enzymes: A Practical Introduction to Structure, Mechanism, and Data Analysis , 2nd ed., Wiley-VCH, New York.
39. Xia, G., Luo, X., Habu, T., Rizo, J., Matsumoto, T., and Yu, H. (2004) Conformation-specific binding of p31(comet) antagonizes the function of Mad2 in the spindle checkpoint. *EMBO J. 23*, 3133–3143.
40. Wood, K. W., Sakowicz, R., Goldstein, L. B. S., and Cleveland, D. W. (1997) CENP-E is a plus end-directed kinetochore motor required for metaphase chromosome alignment. *Cell 91*, 357–366.
41. Nezi, L., Rancati, G., De Antoni, A., Pasqualato, S., Piatti, S., and Musacchio, A. (2006) Accumulation of Mad2-Cdc20 complex during spindle checkpoint activation requires binding of open and closed conformers of Mad2 in *Saccharomyces cerevisiae*. *J. Cell Biol. 174*, 39–51.
42. Meraldi, P., Draviam, V. M., and Sorger, P. K. (2004) Timing and checkpoints in the regulation of mitotic progression. *Dev. Cell 7*, 45–60.